Non-aqueous phase liquid drop formation within a water saturated fracture

Kent M. Pumphrey*, Constantinos V. Chrysikopoulos

Department of Civil and Environmental Engineering, University of California, ET 844C, Irvine, CA 92697-2715, USA

Abstract

This work focuses on the mechanisms of non-aqueous phase liquid (NAPL) drop formation within a single fracture fed from a NAPL reservoir by way of a circular orifice, such as a pore. The fracture is assumed to be fully saturated, the relative wettability of the system is assumed water-wet, and the water velocity profile within the fracture is described by a Poiseuille flow. The size of the NAPL drops is investigated for various water flow velocities and NAPL entrance diameters. A force balancing method was used to determine the radii of detached drops. The drop sizes calculated from the model developed here are shown to be in agreement with available experimental drop size data. It is shown that at low Reynolds numbers the buoyancy force is the dominant force acting on the drop during the formation process and at high Reynolds numbers the viscous forces dominate. A simplified expression relating the geometry of the fractured system to the drop radii is developed from the model equations, and it is shown to predict drop radii that match well with both the model simulations and the available experimental data.
© 2004 Elsevier B.V. All rights reserved.

Keywords: NAPL; Fracture; Drop formation; Drop detachment; Poiseuille flow

1. Introduction

Non-aqueous phase liquids (NAPLs) have played a major role in contaminating aquifers through out much of the industrial world [1]. Typical NAPLs have very low water solubilities and their presence in drinking water is hazardous even at concentrations of just a few parts per billion [2]. NAPLs migrate into aquifers through a number of pathways including fractures that may be imbedded within the bedrock that contains the aquifer. Such fractures have the potential for providing pathways that may lead to enhanced NAPL migration and aquifer contamination that is less accessible to contemporary remediation processes [3]. There are several ways a NAPL can migrate within a fracture; however, it should be noted that not all of the mechanisms associated with this migration are fully understood.

There are numerous publications available in the literature addressing contaminant movement within fractured

bedrock. Kueper and McWhorter [4] examined some of the entry conditions required for a NAPL to enter into a fracture embedded within a clay aquitard. Keller et al. [5] studied the movement of NAPLs within a fracture under two-phase flow conditions and Slough et al. [6] simulated the migration of NAPLs in a discrete-fracture network. VanderKwaak and Sudicky [3], Parker et al. [7] and Rubin et al. [8] analyzed the rates of NAPL dissolution into the aqueous phase and the subsequent contaminant plume movement within rock fractures. The work by James and Chrysikopoulos [9,10], Abdel-Salam and Chrysikopoulos [11] and Chrysikopoulos and Abdel-Salam [12] examined the effects of the various colloid interactions within a fractured medium and how these interactions can alter (increase or decrease) the rate of solute migration. Shikaze et al. [13] examined the movement of vaporized contaminants as they migrate within a fractured geologic medium. However, the formation and migration of NAPL drops within a fracture has not been examined in the literature. Therefore, it is the intent of this work to examine the physical conditions required for NAPL drop formation and to calculate the potential sizes these drops may attain as they form within a water saturated fracture.

---

* Corresponding author.

Nomenclature

A_{eff}	effective area of the drop (L^2)
A_f	area of the NAPL entrance pore (L^2)
$C_{d\alpha}$	drag coefficient for a bounded flow
C_D	drag coefficient for unbounded flow
d	diameter of the NAPL entrance pore (L)
$\bar{d}$	dimensionless NAPL entrance pore diameter
$\tilde{F}$	inertial force (ML/T^2)
$\tilde{F}_B$	buoyancy force (ML/T^2)
$\tilde{F}_D$	drag force (ML/T^2)
$\tilde{F}_L$	lift force (ML/T^2)
$\tilde{F}_M$	momentum force (ML/T^2)
$\tilde{F}_{NI}$	surface tension force at the NAPL/interstitial fluid interface (ML/T^2)
$\tilde{F}_S$	surface tension force (ML/T^2)
$\tilde{F}_V$	viscous force (ML/T^2)
g	gravitational acceleration constant (L/T^2)
h_f	Harkins' correction factor
K	constant
m	exponent
p	constant
Q_d	NAPL volumetric flow rate (L^3/T)
r	drop radius (L)
$\bar{r}$	dimensionless drop radius
r_f	final drop radius (L)
r_0	drop radius at zero interstitial fluid velocity (L)
Re	Reynolds number of the drop
$\overleftarrow{s}$	drop's center position vector (L)
$\hat{s}$	unit position vector for the drop's center (L)
t	time (T)
t_f	time when drop formation is complete (T)
U_{eff}	magnitude of the effective velocity vector (L/T)
$\tilde{U}_{eff}$	effective velocity vector (L/T)
$\hat{U}_{eff}$	unit effective velocity vector
$U(\eta)$	Poiseuille velocity profile of the interstitial fluid (L/T)
U	maximum interstitial fluid velocity (L/T)
V_d	drop volume (L^3)
V_{d0}	drop volume at zero interstitial fluid velocity (L^3)
V_f	drop volume after detachment (L^3)
W	one half the fracture aperture (L)
We	Weber number
x	spatial coordinate in the longitudinal direction (L)
$\hat{x}$	unit vector the x-direction
y	spatial coordinate in the vertical direction (L)
$\hat{y}$	unit vector in the y-direction
Y	dimensionless drop volume

Greek letters

β	relative wettability contact angle
γ	surface tension coefficient (M/T^2)
η	spatial coordinate normal to the fracture wall (L)
$\hat{\eta}$	unit vector normal to the fracture wall (L)
η_D	drop's center coordinate normal to the fracture wall (L)
θ	fracture angular offset
μ_w	absolute viscosity of water (M/LT)
ξ	spatial coordinate in the longitudinal direction (L)
$\hat{\xi}$	unit vector in the longitudinal direction
ξ_D	drop's center longitudinal coordinate (L)
ρ_d	NAPL density (M/L^3)
ρ_w	interstitial fluid density (M/L^3)
ϕ	NAPL entrance angle
ψ	angle of inclination between the drop's center and the η-axis

2. Background

In fractured subsurface formations NAPLs can use fractures as conduits to enhance their spreading. The increased spreading is caused by the higher fluid flow rates that exist within a fracture. Gvirtzman et al. [14], using tritium as a tracer, documented that water traveled at higher velocities within fractures as compared to the water flow rate within the hosting porous matrix. The higher velocities exist because the saturated hydraulic conductivity values of fractures are several orders of magnitude larger than those of the porous rock matrix [15]. These higher hydraulic conductivity values lead to higher fluid flow rates for a given hydraulic gradient. Consequently, fractures provide flow paths that the entrained contaminants can use to migrate faster and further into the subsurface.

NAPLs can enter into a fracture either from the surrounding porous matrix or from any small opening that may intersect the fracture. A NAPL may enter into a fracture when its capillary pressure exceeds the sum of the interstitial fluid pressure within the fracture and the surface tension acting on the NAPL/interstitial fluid interface (see Fig. 1). Once a NAPL has entered a fracture it can either form a single-phase layer that spreads along the fracture wall or form a drop at the entrance point that eventually detaches from its source and enters into the fracture's interstitial fluid. NAPL drops may also be generated when a NAPL layer is exposed to ionic surfactants that exist either naturally or are injected during site remediation efforts [16]. However, this mechanism for drop formation will not be examined in this study.

The final form of an invading NAPL is dependent on the relative wettability of the two fluids that come into contact
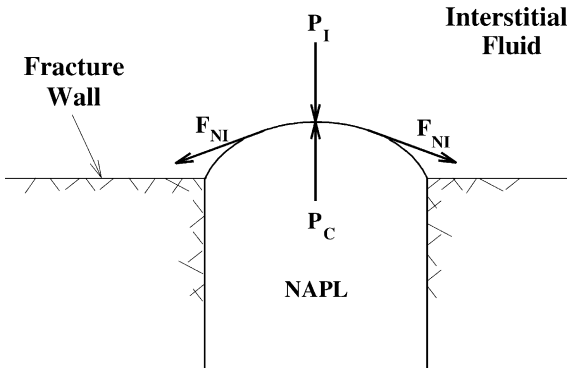
Fig. 1. Schematic illustration of the fluid pressures and surface tension force acting on an exposed NAPL surface as it enters into a fracture (P_C is the capillary pressure, P_I is the interstitial fluid pressure and F_{NI} is the surface tension force at the NAPL/interstitial fluid interface).
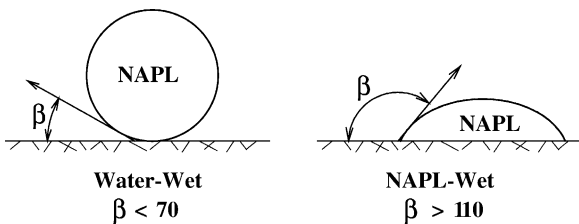

Fig. 2. Schematic illustration of the relative wettability of a NAPL–water–solid system under water-wet and NAPL-wet conditions.

with the fracture wall. The relative wettability is defined by the contact angle, β, which is the angle between the solid and the liquid-liquid interface (see Fig. 2). The contact angle depends on the magnitude of the surface tension forces acting on the NAPL at the NAPL-water-solid contact point. A system is considered water-wet when $\beta < 70°$ and NAPL-wet when $\beta > 110°$. When β is between 70 and 110° the system is considered to be neutral wetting [17]. Generally, water–hydrocarbon systems are considered to be water-wet [18]. However, it has been observed that water–hydrocarbon systems in carbonate rock can be neutral wetting [17]. Consequently, a NAPL entering into a water-wet system is expected to extend into the aperture of the fracture and not spread along the fracture wall, while a NAPL entering a NAPL-wet system is expected to migrate along the fracture walls. This study focuses on a water-wet fracture system that provides the greatest potential for forming NAPL drops.

3. Drop formation within a fracture

The formation of a liquid drop as it enters into a moving fluid is a complicated, three-dimensional process involving moving two-phase fluid interfaces [19]. Traditionally, a problem such as this is examined from a microscopic viewpoint using the Navier-Stokes equation so that the forces acting on fluid interfaces are accurately represented, thus providing the means necessary to calculate the surface de-

formations required to form a drop. However, for Reynolds numbers less than one, the mathematical analysis of this physical system can be simplified greatly, because at these flow conditions a drop's surface does not distort and the drop acts as if it were a solid object [20]. A drop slowly forming from a circular orifice, such as a pore channel intersecting a fracture, can be represented in this fashion. Consequently, the drop formation analysis performed in this work begins with the assumption that the Reynolds number is less than one. This simplification allows for the determination of the radius of a detached drop by examining all of the macroscopic forces acting on the drop's surface during the formation process as the final size of the drop is ultimately dependent on the magnitude and the direction of each of these forces.

The formation of a NAPL drop, as illustrated in Fig. 3, begins the moment that the NAPL enters the fracture and continues as long as the drop remains connected to its source. The drop establishes contact to its source by forming a small neck that connects the body of the drop to the NAPL entrance point. The neck allows the NAPL source to continuously feed the drop while anchoring the drop to the fracture wall. The drop formation is completed when the drop severs its neck and detaches from its source. During the formation process there are four forces acting on the drop. Three of the forces, the buoyancy force, $\bar{F}_B$, the viscous force, $\bar{F}_V$, and the momentum influx force, $\bar{F}_M$, act to move the drop away from its source point. The surface tension force, $\bar{F}_S$, is the only force keeping the drop connected to its source. An illustration showing each of these forces is provided in Fig. 4. The balance of these forces determines the instant when the surface tension force is overwhelmed by the other three forces and ends the drop formation process. Specifying each of these forces provides the means for calculating the instant that the NAPL drop severs its neck. Knowing when the drop detaches from its material source provides the necessary information required for calculating the drop's final size.

4. Definition of forces acting on a forming drop

Newton's Second Law is used to develop the relationship of the macroscopic forces acting on the drop during the formation process and is given by [21]

$$\bar{F} = \bar{F}_B + \bar{F}_V + \bar{F}_M + \bar{F}_S, \tag{1}$$

where $\bar{F}$ represents the drop's inertial force. In order to determine the instant when these forces come into balance, each force must be examined separately.

4.1. Buoyancy force ($\bar{F}_B$)

A buoyancy force is created when the NAPL density differs from the density of the interstitial fluid and is equivalent to the difference between the weight of the drop and
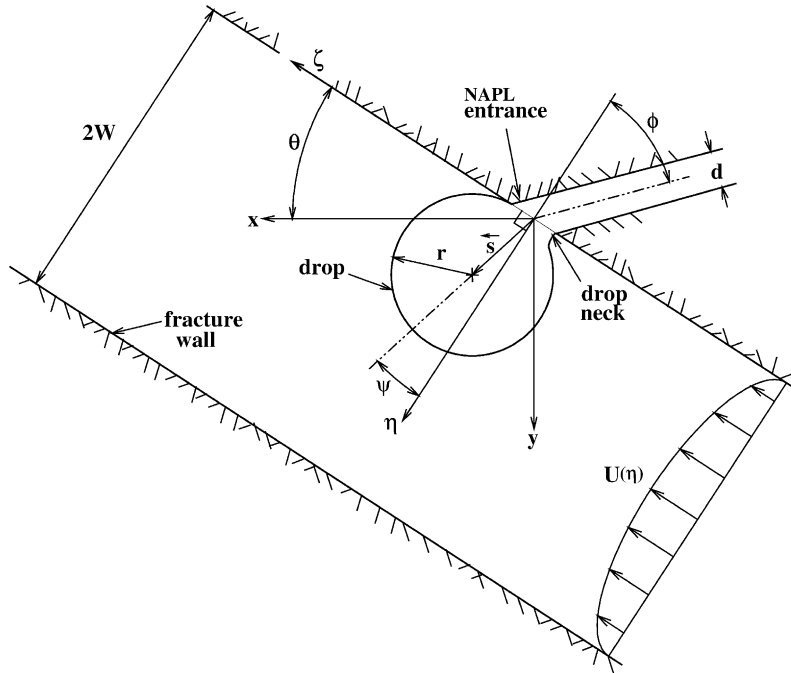
Fig. 3. Schematic illustration of a NAPL drop forming within a uniform, water saturated, two-dimensional fracture.

the weight of the displaced interstitial fluid. The buoyancy force is defined as [22]

$$\bar{F}_B = V_d g (\rho_d - \rho_w) \hat{y}, \tag{2}$$

where V_d is the drop volume, ρ_d the NAPL density, ρ_w the interstitial fluid density, g the gravitational acceleration constant and $\hat{y}$ is the unit vector oriented in the same direction as the gravitational acceleration vector. The drop's volume at any time during its formation process can be approximated from the following equation:

$$V_d = Q_d t, \tag{3}$$

where Q_d is the NAPL volumetric flow rate that is assumed to be constant and t is the elapsed time since the NAPL initially entered the fracture. The value of V_d, as determined by Eq. (3), is only an approximation because a portion of the NAPL that has entered the fracture is contained within the drop's neck. The amount of NAPL contained within the drop's neck is a negligible portion of the overall drop volume and shall be neglected at this point of the analysis. However,

Fig. 4. Schematic illustration of the macroscopic forces acting on a NAPL drop during the drop formation process.

there are correction factors available in the literature that account for the neck volume when computing the drop's final size. An appropriate correction factor will be introduced in a subsequent section.

In this study, the y-coordinate may be offset from the axis normal to the fracture wall. In order to simplify the analysis, the buoyancy force is transformed into a new coordinate system that is aligned with the fracture. The appropriate transformation is give by

$$\hat{y} = \hat{\eta} \cos\theta - \hat{\xi} \sin\theta, \tag{4}$$

where $\hat{\eta}$ is the unit vector in the η-direction (normal to the fracture wall), $\hat{\xi}$ is the unit vector in the ξ-direction (longitudinal direction) and θ is the fracture's angular offset with respect to the x-axis. Substituting the time-dependent relationship (3) into (2) and transforming the resulting buoyancy force equation to the desired coordinate system yields

$$\bar{F}_B = Q_d (\rho_d - \rho_w) g t (\hat{\eta} \cos\theta - \hat{\xi} \sin\theta) \tag{5}$$

4.2. Momentum influx force ($\bar{F}_m$)

During the drop's formation period, momentum is continually added to the drop by the steady influx of NAPL. The force generated by the added momentum acts on the drop in the direction of influx and is considered constant for a constant volumetric flow rate of the NAPL. The equation for the momentum flux force is written as [23]

$$\bar{F}_m = Q_d^2 \frac{\rho_d}{A_f} (\hat{\eta} \cos\phi + \hat{\xi} \sin\phi), \tag{6}$$

where A_f is the area of the NAPL entrance point, and ϕ is the NAPL entrance angle. If the area of the NAPL entrance
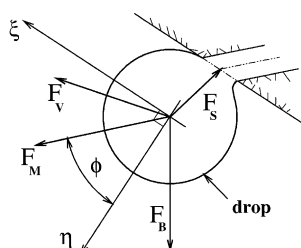
into the fracture is circular then

$$A_f = \frac{\pi}{4}d^2, \tag{7}$$

where d is the diameter of the NAPL entrance point. In view of (7), the expression for the momentum force becomes

$$\breve{F}_m = \frac{4Q_d^2\rho_d}{\pi d^2}(\hat{\eta}\cos\phi + \hat{\xi}\sin\phi). \tag{8}$$

4.3. Viscous force ($\breve{F}_V$)

The viscous force acting on the drop arises from the pressure differential across the drop caused by the flowing interstitial fluid, the viscosity of the fluids and the internal circulation within the drop. The viscous force consists of two components. The first force component, $\breve{F}_D$, drags the drop in the direction of fracture flow and the second component, $\breve{F}_L$, lifts the drop away from the fracture wall. Therefore, the viscous force can be expressed as

$$\breve{F}_V = \breve{F}_D + \breve{F}_L. \tag{9}$$

The drag component of the viscous force is given by [20]

$$\breve{F}_D = \tfrac{1}{2}C_{d\alpha}\rho_w A_{eff}U_{eff}^2\hat{U}_{eff}, \tag{10}$$

where $C_{d\alpha}$ is the drag coefficient for bounded flow, $\hat{U}_{eff}$ is the unit effective velocity vector, U_{eff} is the magnitude of the effective velocity vector and $A_{eff} = \pi r^2$ is the effective area of the drop (where r is the radius of the drop). The drag coefficient accounts for the pressure and viscous forces generated by the modified velocity profile created by the interstitial fluid impinging upon the drop's surface. The effective velocity vector is defined as

$$\tilde{U}_{eff} = U_{eff}\hat{U}_{eff} = \left[U(\eta_D) - \frac{d\xi_D}{dt}\right]\hat{\xi}, \tag{11}$$

where ξ_D is the longitudinal coordinate of the center of the drop, η_D is the coordinate normal to the fracture wall passing through the center of the drop, $d\xi_D/dt$ is the velocity of the drop in the ξ-direction, and $U(\eta_D)$ is the interstitial fluid velocity at the drop's center. Because the drop's neck anchors it to the fracture wall during the formation process, $d\xi_D/dt \approx 0$ and the effective velocity is approximately equal to the interstitial fluid velocity at the location of the drop's center. The interstitial velocity profile is assumed to be a Poiseuille flow, therefore the expression for $U(\eta)$ is given by [20]

$$U(\eta) = \frac{U}{W^2}(2W\eta - \eta^2), \tag{12}$$

where U is the maximum interstitial fluid velocity at the center of the fracture and W is one-half the fracture aperture. The function $U(\eta_D)$ is determined by replacing the independent variable, η by η_D in Eq. (12).

The drag coefficient, $C_{d\alpha}$, is determined from an unbounded flow regime around a solid sphere and then adjusted for the case of bounded flow. This adjustment is necessary because the confining walls of a fracture have an effect on the drag force exerted on a drop. The drag coefficient for unbounded flow about a sphere is [20]

$$C_D = \frac{24}{Re} + \frac{6}{1 + \sqrt{Re}} + 0.4, \tag{13}$$

where Re is the Reynolds number for a drop moving within the fracture and is defined as [20]

$$Re = \frac{\rho_w U(\eta_D)2r}{\mu_w}, \tag{14}$$

where μ_w is the absolute viscosity of water. It should be noted that expression (13) is valid for $0 \leq Re \leq 10^5$. It is assumed that the drop remains spherical through out the formation process as experiments have shown that a drop maintains a spherical shape for drop-to-containment ratios as large as 0.60 [24]. The drag coefficient for bounded flow is defined as [21]

$$C_{d\alpha} = \frac{C_D}{(1 - \bar{r}^2)^3}, \tag{15}$$

where $\bar{r} = r/W$ is the dimensionless radius of the drop.

The lift force generated on a drop is a consequence of the velocity gradient of the interstitial fluid normal to the fracture wall and the asymmetric surface pressure distribution acting on the surface of the drop [25]. Saffman [26] has derived a theoretical expression for the lift force

$$\breve{F}_L = 6.46\mu_w r^2 U(\eta_D)\left(\frac{dU(\eta)}{d\eta}\bigg|_{\eta=\eta_D}\frac{\rho_w}{\mu_w}\right)^{1/2}\hat{\eta}. \tag{16}$$

Although this expression for the lift force was derived for simple shear flow, it is assumed to adequately define the lifting force acting on a drop within the parabolic Poiseuille flow considered in this work. In view of Eqs. (9)–(12) and (16), the viscous force can be expressed as:

$$\breve{F}_V = 6.46\mu_w r^2 U(\eta_D)\left(\frac{2U\rho_w}{W^2\mu_w}(W - \eta_D)\right)^{1/2}\hat{\eta}$$
$$+ \frac{\pi}{2}\rho_w r^2 C_{d\alpha}U^2(\eta_D)\hat{\xi}, \quad \eta_D < W. \tag{17}$$

4.4. Surface tension force ($\breve{F}_S$)

The surface tension force acts on the drop at the drop/fracture wall connection point and attaches the drop to the fracture wall. This force is directed from the center of the drop towards the center of the NAPL entrance point. Assuming that the NAPL entrance point is circular, the expression for this force is [23]

$$\breve{F}_S = -\gamma\pi d\hat{s} = -\gamma\pi d\left(\cos\psi\hat{\eta} + \sin\psi\hat{\xi}\right), \tag{18}$$

where γ is the surface tension coefficient, ψ the angle of inclination between the drop's center and the η-axis (see Fig. 3), and $\hat{s} = \overleftarrow{s}/|s|$ is the unit position vector for the drop's center.

5. Final drop size formulation

The drop formation process ends when the drop severs its neck and begins its migration within the fracture. The moment of drop detachment is defined as the time when Eq. (1) is balanced, or equivalently when

$$\bar{F} = \bar{F}_B + \bar{F}_V + \bar{F}_M + \bar{F}_S = 0. \tag{19}$$

Inserting the mathematical expressions for each of the forces considered into (19) and replacing the coordinate η_D by r yields the following set of equations $\hat{\eta}$-direction:

$$\frac{4Q_d^2\rho_d}{\pi d^2}\cos\phi + Q_d(\rho_d - \rho_w)gt\cos\theta + 6.46\mu_w r^2 U(r)$$

$$\times \left(\frac{2U\rho_w}{W^2\mu_w}(W - r)\right)^{1/2} = \gamma\pi d\cos\psi, \tag{20}$$

$\hat{\xi}$-direction:

$$\frac{4Q_d^2\rho_d}{\pi d^2}\sin\phi - Q_d(\rho_d - \rho_w)gt\sin\theta$$

$$+ \frac{\pi}{2}\rho_w C_{d\alpha} r^2 U^2(r) = \gamma\pi d\sin\psi. \tag{21}$$

Assuming that the forces in the $\hat{\xi}$-direction are balanced during the complete drop formation process, Eq. (21) is valid for all time steps. This assumption provides the necessary relationship for ψ needed to obtain the time when Eq. (20) becomes valid. Consequently the expression for ψ is obtained by rearranging (21) as

$$\sin\psi = \frac{1}{\gamma\pi d}\left\{\frac{4Q_d^2\rho_d}{\pi d^2}\sin\phi - Q_d(\rho_d - \rho_w)gt\sin\theta\right.$$

$$\left. + \frac{\pi}{2}\rho_w C_{d\alpha} r^2 U^2(\eta_D)\right\}. \tag{22}$$

The time, t_f, signifies the moment when the drop formation process has ended. To find t_f Eqs. (20) and (22) are evaluated iteratively at increasing time steps until (20) becomes valid. Once t_f is determined the final drop volume can be calculated by [22]

$$V_f = h_f V_d = h_f Q_d t_f. \tag{23}$$

where V_d is the volume of the drop at the instant of detachment and h_f is the Harkins' correction factor that accounts for the small volume of NAPL left behind at the entrance point as the drop detaches from its source. Assuming that the shape of the detached drop is spherical, V_f can also be expressed as

$$V_f = \frac{4}{3}\pi r_f^3, \tag{24}$$

where r_f is the final drop radius. The Harkins' factor is a curve fitted equation defined as [27]

$$h_f = 1.0 - 0.66023\frac{d}{V_d^{1/3}} + 0.33936\frac{d^2}{V_d^{2/3}},$$

$$0 \le \frac{d}{V_d^{1/3}} \le 0.6, \tag{25}$$

$$h_f = \left\{0.92878 + 0.87638\frac{d}{V_d^{1/3}} - 0.261\frac{E}{V_d^{2/3}}^2\right\}^{-1},$$

$$0.6 < \frac{E}{V_d^{1/3}} < 2.4. \tag{26}$$

A graphical representation of h_f as a function of $d/V_d^{1/3}$ is presented in Fig. 5. Substituting (24) into (23) yields the following expression for the final drop radius

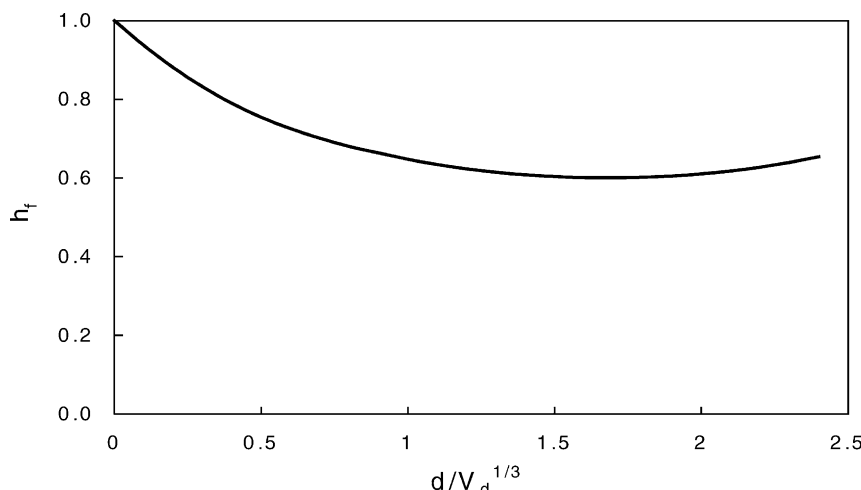$$r_f = \left(\frac{3Q_d}{4\pi}h_f t_f\right)^{1/3}. \tag{27}$$

Fig. 5. Harkins' correction factor as a function of the drop volume at the instant of detachment.

6. Comparison of model predictions to existing experimental data

To verify the accuracy of the theoretical model, calculated drop sizes were compared against experimental data reported by Itoh et al. [23]. This data is the best available experimental representation of a NAPL entering into a moving liquid through a small orifice, though it is a simplified version of an actual system. The Itoh et al. [23] experiments measured the drop diameters generated by a NAPL injected from a nozzle into a flowing stream of water. These experiments represent a simplified version of an ideal system consisting of a NAPL entering a fracture. During each experiment the NAPL injection rate was held constant while the water flow rate was varied from 0 to 30 cm/s. The injection nozzle could be oriented either perpendicular (cross flow) or parallel to the water flow. The following empirical correlation, based on the experimental data, predicting the drop volumes generated for a cross flow configuration was developed by Itoh et al. [23]

$$Y^2 + \frac{9}{64} We^{3/2} Y = 1, \tag{28}$$

where $Y = V_d / V_{d0}$, $We = 4U^2 \rho_w r_0^2 / \gamma d$ is the Weber number, V_{d0} is the drop volume for the cross flow configuration at zero water velocity. V_{d0} can be calculated from the model Eqs. (20)–(27) with the angles θ, ϕ, ψ, plus the interstitial velocity, U, set equal to zero and r_0 (the drop radius at zero water velocity) can be calculated from V_{d0}, assuming that the drop is spherical.

Table 1 shows the comparison of Itoh et al. [23] empirical correlation (28) for a water/benzene system and predictions made by the model Eqs. (20)–(27) derived in this study. The model predictions compare favorably with the correlation of Itoh et al. [23]. Note that the model under-predicts drop radii by up to 0.008 cm (4%) at the lower water velocities and over-predicts drop radii by up to 0.003 cm (3%) at the higher water velocities. Fig. 6 compares graphically the Itoh et al. [23] empirical correlation, the drop radii predictions based on the model derived here and the available experimental data. This figure shows that the radii predicted by the correlation and the theoretical model are contained well within the range of the experimentally measured values. The theoretical model actually predicts drop radii that match the experimental data somewhat better than the correlation of Itoh et al. [23]. The discrepancy between the two predictive models can be attributed to the fundamental difference in their development. The Itoh et al. [23] empirical correlation is based on experimental data, therefore it is system specific; whereas the model Eqs. (20)–(27) are theoretically (mechanistic) derived and are not biased on any particular system.

7. Drop size results and discussion

The interaction of the four forces acting on a drop during the drop formation process dictates the final drop size at the

Table 1
Comparison of the detached drop radii calculated by the theoretical model derived in this study to the Itoh et al. [22] correlation

U_w (cm/s)	$r_{f_{Itoh}}$ (cm)	$r_{f_{study}}$ (cm)	$r_{f_{Itoh}} / r_{f_{study}}$
0	0.2466	0.2466	1.00
1	0.2464	0.2454	1.00
2	0.2454	0.2422	1.01
3	0.2427	0.2371	1.02
4	0.2374	0.2300	1.03
5	0.2290	0.2207	1.04
6	0.2174	0.2096	1.04
7	0.2032	0.1973	1.03
8	0.1875	0.1842	1.02
9	0.1719	0.1710	1.01
10	0.1574	0.1583	0.99
11	0.1445	0.1466	0.99
12	0.1332	0.1359	0.98
13	0.1233	0.1265	0.97
14	0.1147	0.1180	0.97
15	0.1072	0.1105	0.97
16	0.1006	0.1038	0.97
17	0.0947	0.0977	0.97
18	0.0894	0.0925	0.97
19	0.0848	0.0877	0.97
20	0.0805	0.0832	0.97
21	0.0767	0.0791	0.97
22	0.0732	0.0754	0.97
23	0.0700	0.0721	0.97
24	0.0671	0.0689	0.97
25	0.0644	0.0661	0.98

instant of detachment. To illustrate how each force affects the drop formation process, the relative magnitude of the forces acting on a benzene/water drop system as a function of the interstitial fluid velocity are presented in Fig. 7. Note that at low velocities the dominant force acting to overcome surface tension is the buoyancy force. The magnitudes of the lift and drag forces are comparably smaller at the lower interstitial fluid velocities as they are both proportional to this velocity, whereas the buoyancy force is not affected because it is independent of the fluid velocity. As the interstitial velocity increases, the drag and lift forces begin to make larger contributions to the net force counteracting the surface tension force. The increase in the two viscous forces reduces the magnitude of the buoyancy force required to overcome the surface tension force that keeps the drop attached to its source. A smaller buoyancy force corresponds to a smaller drop and is one of the reasons why smaller drops are generated at the higher water velocities. Note that the momentum force remains constant throughout the formation process and is three orders of magnitude lower than the surface tension force. For the system considered here, the momentum force does not play a significant role in drop creation. Furthermore, it is evident from Fig. 7 that the buoyancy force dominates at low velocities, the viscous forces dominate at high velocities and the momentum force does not play a significant role in the drop formation processes.

To evaluate the potential NAPL drop sizes that can be created within a fracture, various drop radii were generated
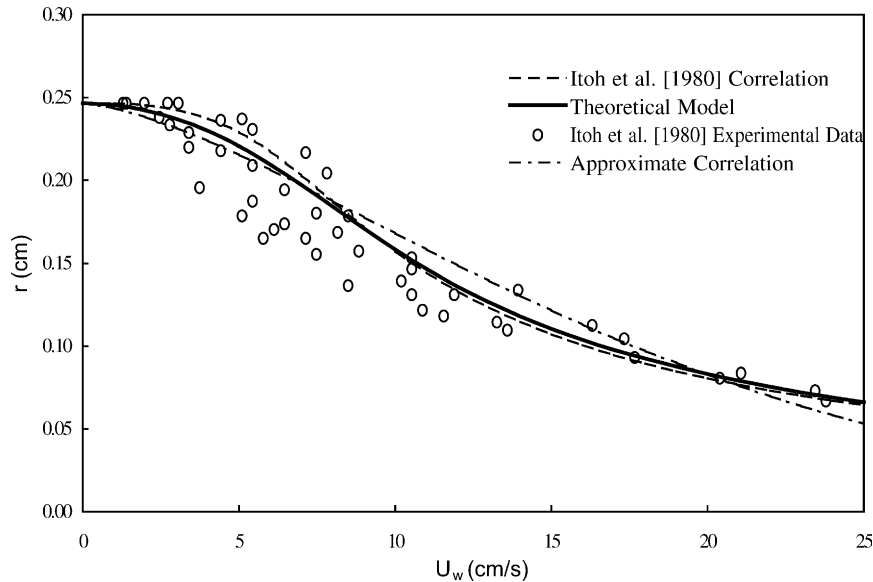
Fig. 6. Graphical comparison of drop radii calculated from the theoretical model, the Itoh et al. [23] correlation, the approximate correlation and the experimental data for benzene drops formed within stream of water flowing perpendicular to the injection nozzle (here $W = 15\,cm$, $Q_d = 0.0070\,cm^3/s$, $d = 0.1\,cm$, $\theta = \phi = 0$, $\rho_d = 0.874\,g/cm^3$, $\rho_w = 0.997\,f/cm^3$).

from the theoretical model Eqs. (20)–(27) for various entrance diameters and water velocities. Assuming that the NAPL is trichloroethylene (TCE) and water is the interstitial fluid, the predicted values of the dimensionless radius $\bar{r}_f$ are presented in Fig. 8. As expected, higher water velocities and/or smaller entrance diameters yielded smaller drop sizes. Fig. 8 also shows that the following approximate relationship between $\bar{r}$ and the entrance diameter, $\bar{d}$, for the water velocities considered, can be obtained

$$\bar{d}^m \approx K\bar{r}, \tag{29}$$

where K is a constant and the exponent m is a function of U and $\bar{d}$. The appropriate expressions for K and m are (for derivation see Appendix A)

$$K = \left[\frac{2g}{3\gamma} W^2 (\rho_d - \rho_w)\right]^{1/3}, \tag{30}$$

$$m \approx \frac{1}{3} - \frac{5U^{3/2}}{\bar{d}^{1/3}\ln(\bar{d})K^3\gamma}(2W\mu_w\rho_w). \tag{31}$$

The value of $\bar{r}$ calculated from (29)–(31) is for the drop radius at the moment of detachment. The final drop radius
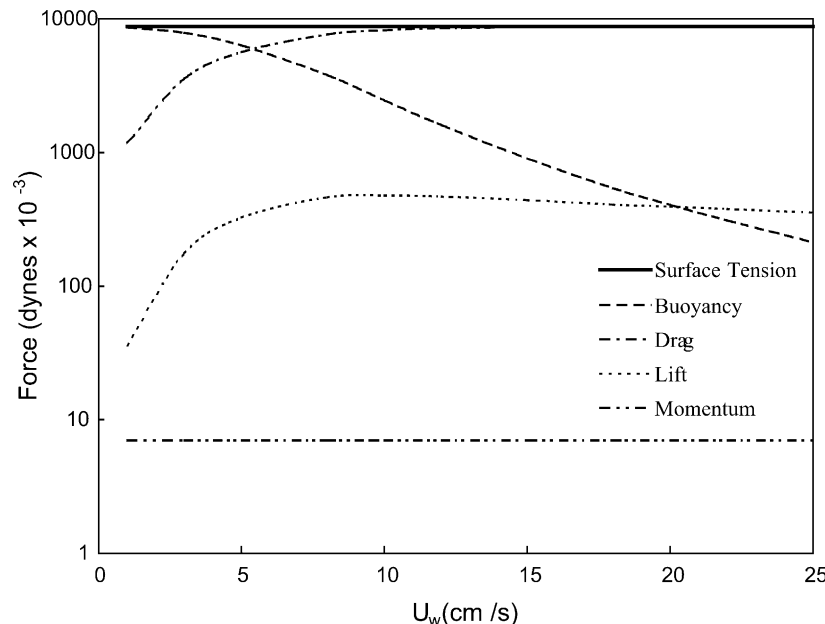

Fig. 7. Graphical comparison of the magnitude of the forces acting on benzene drops at the instant of detachment (here $Q_d = 0.0070\,cm^3/s$, $d = 0.1\,cm$, $\theta = \phi = 0$, $\rho_d = 0.874\,g/cm^3$, $\gamma_{ben} = 28.00\,dyn/cm$).
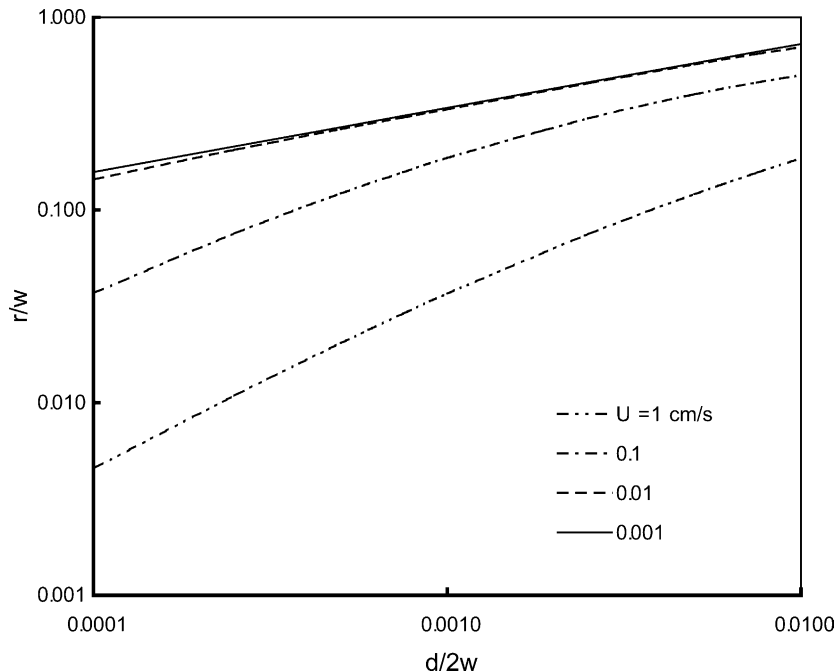
Fig. 8. Graphical comparison of the TCE drop radius generated from the theoretical model for various entrance diameters and interstitial fluid velocities (here $U_{TCE} = 1.0$ m/year, $W = 5$ mm, $\theta = \phi = 0°$, $\rho_d = 1.46$ g/cm^3, $\rho_w = 0.997$ g/cm^3, $\gamma_{TCE} = 29.6$ dyn/cm, $\mu_w = 0.8904$ dyn s/cm^2).

of the detached drop, $\bar{r}_f$, must account for the small amount of NAPL volume left behind at its source and is calculated from the following equation

$$\bar{r}_f = \bar{r} h_f^{1/3}. \tag{32}$$

Table 2 presents the drop radii calculated from the theoretical model (20)–(27) and the approximate correlation (29). The parameters used for the determination of the numerical values listed in Table 2 are: $W = 5$ mm, $\rho_{TCE} = 1.460$ g/cm^3, $\rho_w = 0.997$ g/cm^3, $\gamma_{TCE} = 29.6$ dyn/cm, and $\mu_w = 0.890$ dyn s/cm^2. The approximate correlation produced drop radii that were within ~3% of the radii calculated from the theoretical model. The approximate correlation is also graphically compared to the Itoh et al. [23] experimental data in Fig. 6. Note that the ap-

proximate correlation predicts reasonably accurate drop radii.

8. Summary

This study focused on the formation of NAPL drops contained within a water saturated fracture. The fracture was assumed to be water-wet and the NAPL influx flow rate constant. A force balance method was used to derive a theoretical model that can predict the size of the NAPL drops generated within the fracture. The drop radii predicted from the model equations derived in this work were compared to existing experimental data and a strong correlation between the calculated radii and the data was shown to exist. Model simulations indicated that the drop radii decreased as the NAPL entrance diameters decreased and/or interstitial velocity increased. Furthermore, a simple approximate correlation for radius estimation of NAPL drops formed within a fracture was developed. The drop radii calculated from the approximate correlation developed here were within 3% of the radii calculated from the theoretical model and compared well with the available experimental data.

Table 2
Calculated exponent m values and comparison of radii calculated from the approximate correlation and the theoretical model for various interstitial velocities

U_w (cm/s)	$\bar{d}$	m	$\bar{r}_{f_{corr}}$	$\bar{r}_{f_{model}}$	$\bar{r}_{f_{corr}}/\bar{r}_{f_{model}}$
0.1	0.005	0.403	0.400	0.399	1.00
	0.001	0.425	0.180	0.186	0.97
	0.0005	0.439	0.121	0.122	0.99
0.01	0.005	0.336	0.574	0.570	1.01
	0.001	0.336	0.333	0.334	1.00
	0.0005	0.337	0.263	0.263	1.00
0.001	0.005	0.333	0.580	0.579	1.00
	0.001	0.333	0.339	0.339	1.00
	0.0005	0.333	0.269	0.269	1.00

Appendix A

Both K and m present in Eq. (29) can be approximated from Eq. (20) by neglecting the momentum force, assuming the inclination angle, ψ, is small and setting the angles θ and

ϕ equal to zero. Applying these assumptions to (20) yields the following expression

$$\pi\gamma\bar{d} = \tfrac{2}{3}\pi g W^2(\rho_d - \rho_w)\bar{r}^3 + 3.23U^{3/2}(2-\bar{r})\bar{r}^3$$
$$\times \{2W\rho_w\mu_w(1-\bar{r})\}^{1/2} \tag{A.1}$$

In view of the following MacLaurin expansion [28]

$$\sqrt{1-\bar{r}} = 1 - \tfrac{1}{2}\bar{r} - \tfrac{1}{8}\bar{r}^2 - \tfrac{1}{16}\bar{r}^3 - \cdots , \tag{A.2}$$

Eq. (A.1) can be simplified by expanding and taking the cube root as follows:

$$\bar{d}^{1/3} = \left\{\frac{2g}{3\gamma}W^2(\rho_d - \rho_w) + 6.46\frac{U^{3/2}}{\pi\gamma}(2W\mu_w\rho_w)^{1/2}\right.$$
$$\left. \times \left(1 - \bar{r} + \tfrac{1}{8}\bar{r}^2 - \cdots \right)\right\}^{1/3}\bar{r}. \tag{A.3}$$

If the exponent m can be expressed as

$$m = \tfrac{1}{3} + f, \tag{A.4}$$

where f is a function to be determined, then Eq. (29) can be expressed as

$$\bar{d}^m = \bar{d}^{1/3}\bar{d}^f \approx K\bar{r}. \tag{A.5}$$

Comparing (A.5) to (A.3) the following relationship is obtained

$$\frac{K}{\bar{d}^f} = \left\{\frac{2g}{3\gamma}W^2(\rho_d - \rho_w) + 6.46\frac{U^{3/2}}{\pi\gamma}(2W\mu_w\rho_w)^{1/2}\right.$$
$$\left. \times \left(1 - \bar{r} + \tfrac{1}{8}\bar{r}^2 - \cdots \right)\right\}^{1/3}. \tag{A.6}$$

Setting $K = [(2g/3\gamma)W^2(\rho_d - \rho_w)]^{1/3}$ and substituting into (A.6) yields

$$\bar{d}^{-f} = \left\{1 + 6.46\frac{U^{3/2}}{K^3\pi\gamma}(2W\mu_w\rho_w)^{1/2}\right.$$
$$\left. \times \left(1 - \bar{r} + \tfrac{1}{8}\bar{r}^2 - \cdots \right)\right\}^{1/3}. \tag{A.7}$$

Taking the natural log of (A.7) yields

$$f = -\frac{1}{3\ln(\bar{d})}\ln\left\{1 + 6.46\frac{U^{3/2}}{K^3\pi\gamma}(2W\mu_w\rho_w)^{1/2}\right.$$
$$\left. \times \left(1 - \bar{r} + \tfrac{1}{8}\bar{r}^2 - \cdots \right)\right\}. \tag{A.8}$$

Eq. (A.8) can be simplified by first assuming that $\bar{r}$ is a large multiple of $\bar{d}$ and by approximating the portion of (A.8) containing the $\bar{r}$ terms in the parenthesis to $\approx p\bar{d}^{-1/3}$ (where p is a constant). Utilizing the relationship $\ln(1 + b) \approx b$ for $b \ll 1$ [28] yields this expression for f

$$f \approx -\frac{5U^{3/2}}{\bar{d}^{1/3}\ln(\bar{d})K^3\gamma}(2W\mu_w\rho_w)^{1/2}. \tag{A.9}$$

Substituting (A.9) into (A.4) yields the desired expression

$$m \approx \frac{1}{3} - \frac{5U^{3/2}}{\bar{d}^{1/3}\ln(\bar{d})K^3\gamma}(2W\mu_w\rho_w)^{1/2}. \tag{A.10}$$

References

[1] C. Khachikian, T.C. Harmon, Non-aqueous phase liquid dissolution in porous media: Current state of knowledge and research needs, Transport Porous Media 38 (1-2) (2000) 3–28.

[2] J.W. Mercer, R.M. Cohen, A review of immiscible fluids in the subsurface: properties, model characterization and remediation, J. Contam. Hydrol. 6 (1990) 107–163.

[3] J.E. VanderKwaak, E.A. Sudicky, Dissolution of non-aqueous-phase liquids and aqueous-phase contaminant transport in discretely-fractured porous media, J. Contam. Hydrol. 23 (1996) 45–68.

[4] B.H. Kueper, D.B. McWhorter, The behavior of dense, nonaqueous phase liquids in fractured clay and rock, Ground Water 29 (5) (1991) 716–728.

[5] A.A. Keller, M.J. Blunt, P.V. Roberts, Behavior of nonaqueous phase liquids in fractured porous media under two-phase flow conditions, Transport Porous Media 38 (2000) 189–203.

[6] K.J. Slough, E.A. Sudicky, P.A. Forsyth, Numerical simulation of multiphase flow and phase partitioning in discretely fractured geologic media, J. Contam. Hydrol. 40 (1999) 107–136.

[7] B.L. Parker, R.W. Gillham, J.A. Cherry, Diffusive disappearance of immiscible-phase organic liquids in fractured geologic media, Ground Water 32 (1994) 805–820.

[8] H. Rubin, K. Rathfelder, L.M. Abrida, Modeling quasi-steady NAPL dissolution in fractured permeable media, J. Environ. Eng. 123 (3) (1997) 25–216.

[9] S.C. James, C.V. Chrysikopoulos, Transport of polydisperse colloid suspensions in a single fracture, Water Resour. Res. 35 (3) (1999) 707–718.

[10] S.C. James, C.V. Chrysikopoulos, Transport of polydisperse colloids in a saturated fracture with spatially variable aperture, Water Resour. Res. 36 (6) (2000) 1457–1465.

[11] A. Abdel-Salam, C.V. Chrysikopoulos, Analytical solutions for one-dimensional colloid transport in saturated fractures, Adv. Water Resour. 17 (1994) 283–296.

[12] C.V. Chrysikopoulos, A. Abdel-Salam, Modeling colloid transport and dispersion in saturated fractures, Colloids Surf. A: Physicochem. Eng. Asp. 121 (1997) 189–202.

[13] S.G. Shikaze, E.A. Sudicky, C.A. Mendoza, Dense vapour migration in discretely fractured geologic media, Water Resour. Res. 30 (7) (1994) 1993–2009.

[14] H. Gvirtzman, M. Magaritz, Y. Kanfi, L. Carmi, Matrix and fissure water movement through unsaturated calcareous sandstone, Transport Porous Media 3 (1988) 343–356.

[15] A. Abdel-Salam, C.V. Chrysikopoulos, Unsaturated flow in a quasi-three-dimensional fractured medium with spatially variable aperture, Water Resour. Res. 32 (6) (1996) 1531–1540.

[16] V.L. Kolev, I.I. Kochijashky, K.D. Danov, P.A. Kralchevsky, G. Broze, A. Mehreteab, Spontaneous detachment of oil drops from solid substrates: governing factors, J. Colloid Interface Sci. 257 (2003) 357–363.

[17] D.C. Gooddy, J.P. Bloomfield, G. Harrold, S.A. Leharne, Towards a better understanding of tetrachloroethane entry pressure in the matrix of Permo-Triassic sandstones, J. Contam. Hydrol. 59 (2002) 247–265.

[18] P.A. Domenico, F.W. Schwartz, Physical and Chemical Hydrology, John Wiley & Sons, 1990.

[19] I. Kim, Y. Kamotani, S. Ostrach, Modeling bubble and drop formation in flowing liquids in microgravity, AIChE J. 40 (1) (1994) 19–28.

[20] F.M. White, Viscous Fluid Flow, second ed., McGraw-Hill, Boston, MA, 1991.

[21] I. Kim, Modeling of bubble and drop formation in flowing liquids in terrestrial and microgravity environments, Ph.D. Dissertation, Case Western Reserve University, Cleveland, OH, 1992.

K.M. Pumphrey, C.V. Chrysikopoulos / Colloids and Surfaces A: Physicochem. Eng. Aspects 240 (2004) 199–209

209

[22] G. Scheele, B. Meister, Drop formation at low velocities in liquid-liquid systems, AIChE J. 14 (1) (1968) 9–15.

[23] R. Itoh, Y. Hirata, K. Inoue, Y. Kitagawa, Formation of a liquid drop at a single nozzle in a uniform stream, Int. Chem. Eng. 20 (1980) 616.

[24] A. Borhan, J. Pallint, Pressure driven motion of drops and bubbles through cylindrical capillaries, Ind. Eng. Chem. Res. 37 (1998) 3748–3759.

[25] R. Eichhorn, S. Small, Experiments on the lift and drag of spheres suspended in a Poiseuille flow, J. Fluid Mech. 20 (1964) 513–527.

[26] P. Saffman, The lift on a small sphere in a slow shear flow, J. Fluid Mech. 22 (2) (1965) 385–400.

[27] R. Clift, J.R. Grace, M.E. Weber, Bubbles, Drops, and Particles, Academic Press, New York, 1978.

[28] W.H. Beyer, Standard Mathematical Tables, 28th ed., CRC Press, Boca Raton, FL, 1987.